870154

Effect of Speed, Load, and Location on Heat Transfer in a Diesel Engine Measurements and Predictions

Thomas Morel and Syed Wahiduzzaman
Integral Technologies Inc.
Dale R. Tree and David P. DeWitt
School of Mechanical Engineering
Purdue Univ.
West Lafayette, IN

ABSTRACT

An experimental study was conducted to measure the heat transfer in a direct injection 2.3 & single cylinder diesel engine. The engine was operated at speeds ranging from 1000 to 2100 RPM and at a variety of loads. The heat transfer was measured using a total heat flux probe, operating on the principle of a thin film thermocouple, sensitive to both the convective and radiative heat flux. The probe was located in the head at two locations: opposite the piston bowl and opposite the piston crown (squish region). The measurements showed about twice as large peak heat flux in the bowl location than in the crown location for fired conditions, while under motoring conditions the relationship was reversed and the peak heat flux was slightly higher in the crown position. The experimental profiles of total heat flux were compared to the predictions obtained using a detailed thermodynamic cycle code, which incorporates highly resolved models of convective and radiative heat transfer. The predictions were found to be in very good agreement with the measurements, both in magnitude and in trends with engine load and speed. The model was found to reproduce very well the observed spatial variations in peak heat flux between the two head locations.

ENGINE HEAT TRANSFER plays an important role in engine design. This is because it affects engine performance due to losses of available energy, and it also affects gas temperatures and through them combustion rate, emissions formation, knock, etc. A separate area of importance is the thermal loading of engine structural components, and the optimization of engine cooling systems.

Taking engine cooling as an example, one can note that its optimization requires the solution of the coupled problem of heat transfer from gases to walls and of heat conduction through the structure. The heat conduction portion of such a calculation can be carried out to any desired accuracy, using finite element models (FEM). By contrast, gas-to-wall heat transfer modeling is still in a developmental state. This presents a major stumbling block, since the gas-to-wall heat transfer correlations are needed to provide the necessary boundary conditions for the FEM codes. The calculated temperature field in the structure depends very critically on these boundary conditions, which must be well grounded in physics, if they are to provide an accurate description of the heat flux rates and of their spatial and temporal variation within the combustion chamber. Inadequacies in gas-to-wall heat transfer modeling also reflect themselves in inaccurate values of basic quantities such as thermal efficiency, power, and exhaust temperature and volumetric efficiency.

In an attempt to advance the state of the art in heat transfer modeling, a comprehensive research program has been carried out in order to develop better methods for evaluating the effects of heat transfer on in-cylinder processes and for establishing accurate boundary conditions for engine component FEM calculations. This program followed two parallel paths. One was analytical, involving the development of a flow-based convective heat transfer model (Morel and Keribar, 1985) and a detailed zonal heat radiation model (Morel and Keribar, 1986). The other path was experimental; in which crank-angle resolved heat transfer data were obtained in a single-cylinder direct injection diesel engine. This paper provides an overview of the models used, describes in detail the experimental part of the program, and presents comparisons between the measured and calculated heat fluxes.

MODELING OF GAS PHASE HEAT TRANSFER

Previous Convective Heat Transfer Models. The need for predictive capability to estimate engine heat transfer rates has been recognized for a long time, and first models suggested for this purpose date back over 60 years.

The models that are currently the most widely used are those due to Annand (1963) and Woschni (1967). Both of these models are based on Nusselt/ Reynolds number correlations, in which the characteristic velocities scale with mean piston speed rather than with actual in-cylinder flow velocities. These models have no spatial resolution, and they ascribe the same value of the heat transfer coefficients to all of the in-cylinder surfaces. The constants used in the model are to be adjusted from engine to engine, and Annand (1963) suggests a range from 0.35 to 0.80 according to "intensity of motion in the region considered."

It is clear that a successful convective heat transfer model must take into account all of the key in-cylinder fluid motions such as: intake flows, swirl, squish, turbulence, and injection and combustion generated motions. Also the model has to provide spatial resolution capable of differentiating between various in-cylinder surfaces. This has been recognized and there has been a gradual evolution from simple correlations towards flow-based models as reviewed eg. in Morel and Keribar (1985). However, none of the models available in the literature incorporated the effect of all of the significant in-cylinder motions, nor did they provide the needed spatial resolution.

Present Convective Heat Transfer Model. The present model attempts to account for all of the important in-cylinder motions, and introduces a differentiation between the combustion chamber surfaces. The model is global in nature, but it incorporates much more physics than previous models and thus it is expected to require much less adjustment from engine to engine or from one combustion chamber shape to another than previous models. In fact, the model has no adjustable constants. It has been used on a range of engines from small high swirl diesels to a locomotive size diesel, and the global, cycle averaged heat rejection levels it predicted have been found to be in good agreement with the heat rejection levels observed in test cell experiments.

The model is based on well-established boundary layer concepts. It calculates velocities and turbulence adjoining each of a number of resolved individual in-cylinder surfaces and from these it determines the local transfer coefficients through Colburn analogy. The required skin friction coefficient is obtained directly from literature boundary layer correlations. To calculate the flow velocities, the flow model divides the combustion chamber volume into three regions (for diesel applications only; a more involved approach is taken for S.I. engines). One region is above the piston crown (squish region), one above the piston bowl and the third one is inside the bowl (Figure 1). In each of the regions the model solves an equation for conservation of angular momentum and two equations for the k-ε turbulence model. The resulting heat transfer coefficients calculated for a piston are shown in Figure 2, showing their values on the center portion of the head, the perimeter portion of the head, and on the liner. One may observe that these values vary strongly from surface to surface and in addition, the relative magnitudes of the heat transfer coefficients change

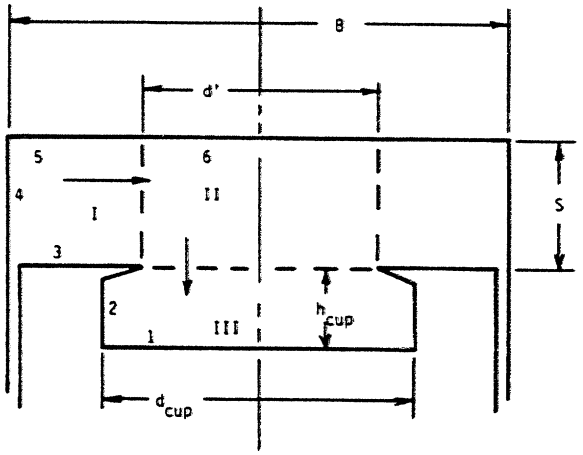

Figure 1. Flow regions appropriate for typical bowl-in-piston diesel engine geometries. Arrows indicate flow direction during compression stroke. Roman numbers refer to flow regions; arabic numbers refer to the elementary surfaces bounding those regions.

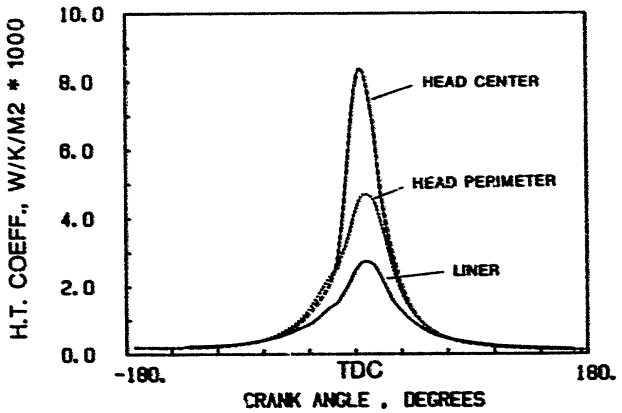

Figure 2. Distribution of heat transfer coefficients on various in-cylinder surfaces.

throughout the cycle. This reflects the changes in the flow velocities adjoining the individual surfaces. When one averages the heat transfer coefficients over all of the surfaces, one can compare the resulting curve to the Annand correlation, which is meant to be applied uniformly to all surfaces. This has been done in Figure 3, where the coefficient of the Annand's correlation has been adjusted in order to give the same cycle-integrated heat rejection for the whole cylinder. It is seen that the flow-based model exhibits sensitivity to the in-cylinder flow development: it produces high values of heat transfer coefficients during intake due to the highly turbulent intake flows; it calculates high heat transfer coefficients near firing TDC due to squish, compression generated turbulence, and injection and combustion motions; finally it calculates low heat transfer coefficients during the relatively quiescent expansion and exhaust periods. By contrast, the Annand correlation shows none of these flow-related features.

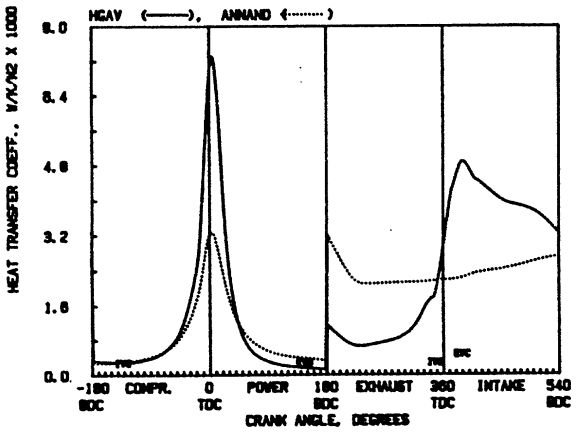

Figure 3. Area averaged heat transfer coefficient; comparison of flow-based model to Annand correlation.

Previous Radiation Heat Transfer Models. In order to calculate diesel engine radiation heat transfer, which is primarily due to soot, one must model these basic variables: soot loading (or soot volumetric fraction) in the combustion gases, radiation temperature and spatial distribution of the radiation heat transfer along combustion chamber walls. Most of the models of radiation used today provide none of the above variables, but calculate radiation heat flux as proportional to the fourth power of the mass-averaged gas temperature, make no account of soot loading, and make radiation flux uniform over all in-cylinder surfaces. The use of mass-averaged temperature is grossly incorrect, giving results that are about 10 times too low, requiring the use of large ad-hoc multipliers to compensate for it. More recently, there have been attempts to correct this situation, but none of these address all of the three basic variables simultaneously (see review in Morel and Keribar, 1986).

Present Radiation Heat Transfer Model. Due to soot formation during diesel combustion, thermal radiation from gases to surrounding combustion chamber surfaces is a significant component of heat transfer. Instantaneous and mean levels of heat radiation are functions of the volume and distribution of burning gas, amount of soot present in the burning gas, combustion chamber geometry, and also of surface emissivities and temperatures. The heat radiation model takes into account all of these dependencies (Morel and Keribar, 1986). The soot concentration levels are calculated using a kinetic model, which provides rates for soot formation and subsequent burnup as a function of engine parameters and crank angle. The spatial distribution of the heat radiation can be calculated from the volume and shape of the burned zone. The burned zone volume is calculated from the cycle thermodynamic simulation, and its shape and location are obtained from an empirically based geometric model. All soot is assumed to be contained within the burned gas. The spatial distribution also includes the effects of chamber geometry through the calculation of the actual optical thicknesses as seen from one surface when viewing another, or when viewing the burned zone. This is accomplished through the use of a zonal radiation model, which divides the combustion chamber surface into seven individual subsurfaces. This model also represents the attenuation of radiation from one surface to another, as it passes through the absorbing burned zone, and accounts for multiple reflections of incident radiation from one surface to another.

Engine Simulation. All predictions presented here were generated using a comprehensive engine design analysis code, described in previous publications (see Morel et al, 1986).

EXPERIMENTAL SETUP

Engine. The experimental part of this work was performed on a Cummins single cylinder engine based on the 14-liter, NH-series heavy-duty truck engine. Bore and stroke are 140 mm by 152 mm and the compression ratio is 15.7:1. The combustion chamber is quiescent and features centrally located, multi-jet direct injection into a shallow mexican hat piston cup which forms the principal part of the combustion chamber. A schematic drawing of the piston cup is shown in Figure 4. The injector is a production eight-orifice Cummins unit injector, cam/pushrod driven, operating on the Cummins P-T system. Injection timing can be adjusted by a special camshaft mechanism and is measured through a strain-gaged injector link

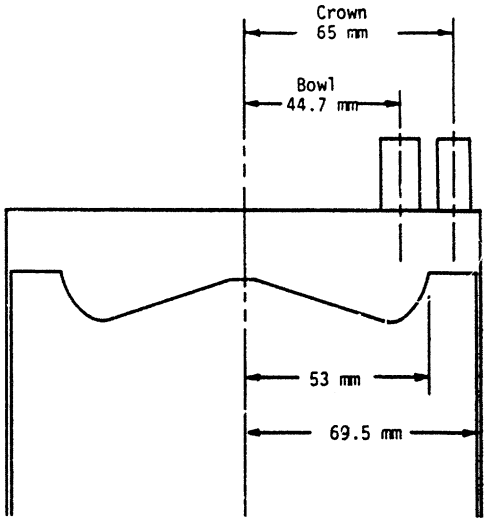

Figure 4. Piston bowl shape and probe locations.

rod. Supercharged operation is accomplished by supplying regulated high-pressure air from an external compressor and accumulator to an intake plenum. This air also can be heated to reproduce typical levels of intake air temperature. Backpressure is controlled by a valve in the exhaust line. Although the engine normally has two intake and two exhaust valves, one intake valve was removed to accommodate instrumentation. Since the engine breathes very freely, this modification has very little effect on air consumption at low rpm. At higher speeds the inlet restriction resulting from using only one valve is offset by increasing inlet boost slightly until the desired air flow is attained.

The engine is supported by external circuits for fuel, lubrication oil and coolant. All fluids can be cooled or heated as required to maintain desired temperatures to the engine. Engine output is absorbed by a Westinghouse DC electric dynamometer rated at 56 kW from 2000 to 5000 rpm. The dynamometer also can supply 45 kW of motoring power over the 1800 to 5000 rpm range.

Instrumentation and Experimental Techniques.

The engine combustion chamber is accessible to the probes through two locations provided at the cylinder head. The first probe access views the squish region and the other location views the deepest section of the piston bowl. This access was created by removing an inlet valve and replacing it with a mounting insert. The locations of the two probes are shown in Figure 5, which displays a section through the head at the valve head plane. The probe accesses were designed to be compatible with both AVL pressure transducer QP505) and Medtherm fast response thermocouple.

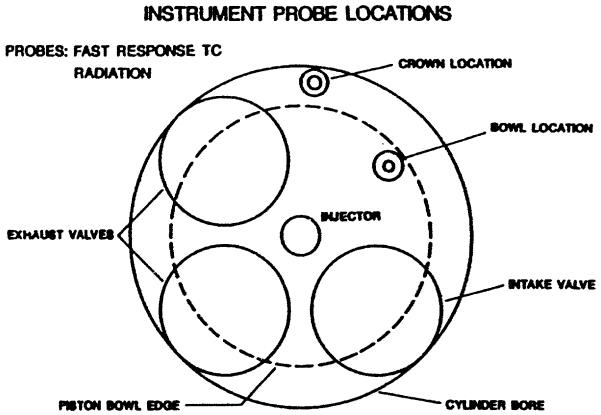

Figure 5. Section through engine head at the valve plane. showing probe locations.

The Medtherm total heat flux probe contains both a fast-response surface thermocouple and a sub-surface thermocouple located 5 mm below the surface. For fast response surface measurements the probe incorporates an electrically insulated thin nickel wire passing through a pure iron cylinder. The nickel wire and the iron cylinder are electrically connected by a thin nickel plating which forms a fast-response thermocouple junction at the probe surface. The sub-surface thermocouple is provided by welding a nickel wire onto the iron cylinder 5 mm from the plated end. The above assembly is swaged into a pure iron body whose external dimensions are compatible with the access provided for AVL pressure transducers. A common iron lead is attached to the iron body to complete the thermocouple lead wire set. The combination of the central nickel wire and the common iron lead attached to the iron body forms the surface thermocouple; whereas the in-depth nickel wire and the common iron lead forms the sub-surface thermocouple.

An experiment was devised to estimate the time constant of the Medtherm heat flux probes. A Nd:Yag laser was used as an energy source to rapidly deposit heat on the sensing face of the heat flux probe. The laser used had a nominal pulse width of 10nsec and pulse energy of 10mJ. It was operated at 20 Hz repetition rate and the thermocouple response was observed in an oscilloscope triggered by a pulse synchronous with the Q-switch of the laser. By recording the rise time of the voltage signal, one can estimate the time constant of the heat flux gauge. It was found that the constant of the probe was between 2 and 3 μsec, which is more than an order of magnitude smaller than that required to resolve in-cylinder heat flux on a crank angle basis.

Both the indepth and the surface thermocouples are provided with differential leads to

minimize signal contamination by extraneous noises. The surface thermocouple voltage is measured in terms of the difference of the two thermocouple (surface and indepth) signals. This enables use of a higher amplifier gain (typically 5k - 10k) in absence of large D.C. offset. The indepth thermocouple output is measured in absolute terms.

A dedicated data acquisition system was built around a PDP 11/23 CPU, an ADAC Corporation 1023FT-1622DMA A/D conversion system and DEC DRV11 clock. The system has 1 megabyte of solid-state memory. Since a portion of the memory is used for the I/0 and data management system, about 800 Kbytes is available for data storage, which corresponds to 6 to 7 runs. In practice, however, more consecutive runs are possible since data is continuously being transferred in the background to the mainframe computer, thereby freeing up memory space. The probe data was sampled at 0.60 CA resolution.

The A/D converter has a dynamic range of -10V and +1OV. To enable fuller utilization of the dynamic range, the analog signals of the heat flux gage are amplified before being fed into the data acquisition system. The amplifier used is a D.C. -coupled differential amplifier (AM 502, Tektronics) having gains up to 100 k with selectable upper and lower -3 db points. The maximum upper -3 db points is 1 MHz and is operated at 10 kHz.

Heat Flux Data Reduction Scheme: In a typical operation, seventeen cycles of data were collected at 0.6 CA resolution for each of the operating conditions. The data reduction was performed on the cycle averaged surface thermocouple signal, to which was added the averaged indepth thermocouple signal to obtain the absolute voltage. This voltage was converted into temperature by interpolating a thermocouple calibration table. To eliminate high frequency noise, the temperature-crankangle record was then smoothed by a sliding least square (cubic, 20 CA interval) fit. The smoothed signal was decomposed into its harmonics by choosing 512 equally spaced points and applying Fast Fourier Transform (FFT). The first 200 harmonics were retained to calculate the cyclic heat flux rate using a 1-D heat conduction formula (Eckert and Drake, 1972):

$$Q_w = k/L\,(T_w - T_d) + k \sum_{1}^{m} \sqrt{(\omega n/\alpha)}\,[A_n \cos(n\omega t - \pi/4) - B_n \sin(n\omega t - \pi/4)]$$

where

k = thermal conductivity of the heat flux gage
L = distance between indepth and surface thermocouples
T_w = average surface temperature
T_d = indepth temperature
ω = 0.5 x angular speed of the engine
α = thermal diffusivity of the heat flux gage
m = number of harmonics retained

The above equation is strictly valid for cases where material properties are not functions of temperature. Although the thermal diffusivity and the conductivity of pure iron (material of the heat flux gage) vary with temperature, it is reasonable to assume that within the penetration depth the temperature, and the properties, are uniform. Hence, the above equation is still valid provided property values at the operating temperature are used. The correction factor that has to be applied to the unsteady portion of the heat flux calculated with room temperature properties is given by

$$F_c = \sqrt{(k\rho c)_o/(k\rho c)_r}$$

where p and c are density and specific heat, respectively, and o and r pertain to operating and room temperature, respectively. This correction factor may be deduced from a one-dimensional exact solution (see eg. Eckert and Drake, 1972).

ENGINE TEST MATRIX

The engine tests were carried out over a broad range of engine operating points representing typical conditions for a turbocharged heavy-duty diesel. To make these conditions realistic, engine simulations were made of the Cummins six-cylinder NH engine on which the single cylinder test engine is based. The specific multi-cylinder engine simulated was the NTC-350 for which Cummins Engine Company supplied detailed engine description, turbo-charger maps, and test data. The simulations were carried out using the same engine design analysis code used for the predictions of radiation heat flux. After correlation with the Cummins-supplied test data, the code was used to calculate operating conditions--intake pressure and temperature, exhaust pressure--at four engine speeds and several loads at each speed to form the test matrix shown in Table I. This assured that all of the operating points were realistic steady-state points of an actual heavy-duty highway diesel engine. Due to dynamometer limitations the peak loads were limited at the lower engine speeds below the full load values. Also, the values given in Table I are those actually observed during the experiments, and differ in minor ways from the target values determined by the simulation.

RESULTS

Motored Runs. In this set of experiments, the engine was motored at four different speeds 1000, 1300, 1700 and 2100 rpm. Four sets of data were acquired at each speed: at two

Speed rpm	Nominal Load %	IMAP bar	IMAT °K	EMAP bar	A/F	dOI °BTC
2100	100	2.45	355	2.09	31.8	23
2100	75	1.86	340	1.74	33.7	18
2100	50	1.60	349	1.53	40.8	13.5
2100	25	1.25	337	1.32	56.8	9.5
1700	88	2.07	349	1.62	33.0	21
1700	50	1.53	355	1.36	40.1	14
1700	25	1.27	356	1.21	65.9	9
1300	75	1.59	331	1.42	27.0	21.5
1300	50	1.30	326	1.26	29.6	17
1300	35	1.21	340	1.19	37.6	13
1300	25	1.12	334	1.17	45.6	11
1000	75	1.36	342	1.22	18.8	24.5
1000	50	1.20	344	1.14	28.2	16
1000	25	1.09	348	1.12	47.2	10.5

Table 1. Engine operating conditions for the firing runs.

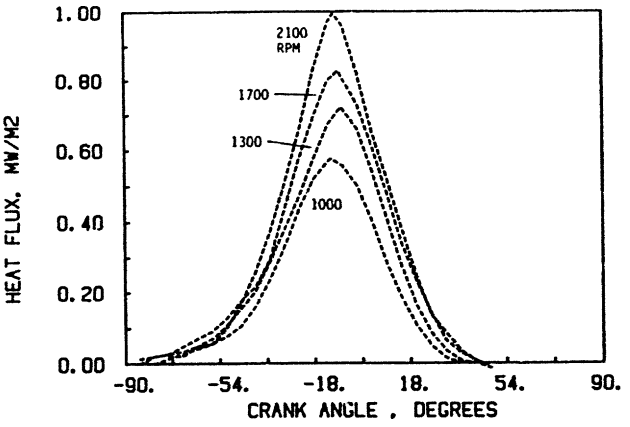

Figure 6b. Measured heat flux at crown location, motoring operation at four engine speeds, P_{int} = P_{exh} =1.2 bar.

different probe locations and at two different intake pressures of 1.2 and 2.0 bar respectively. The engine back pressure was always set equal to the intake pressure.

Figure 6a shows the results obtained at the bowl location (probe installed in the head in the location facing the bowl). The heat flux is seen to increase with increasing speed due to increasing intensity of in-cylinder gas motions. A similar result is obtained at the crown location (Figure 6b), except that the magnitude of the heat flux is somewhat higher. The heat flux levels obtained at the higher intake pressure were about 50% higher, but otherwise they were quite similar to those shown in Figure 3. The curves of the heat flux display asymmetry, in that they have a smaller slope during the compression stroke than during the expansion stroke. This characteristic behavior had been already observed by previous investigators, eg. by Dao et al (1973) and Annand and Pinfold (1980), and its origin lies in the gradually decreasing intensity of in-cylinder motions caused by wall friction and turbulence decay.

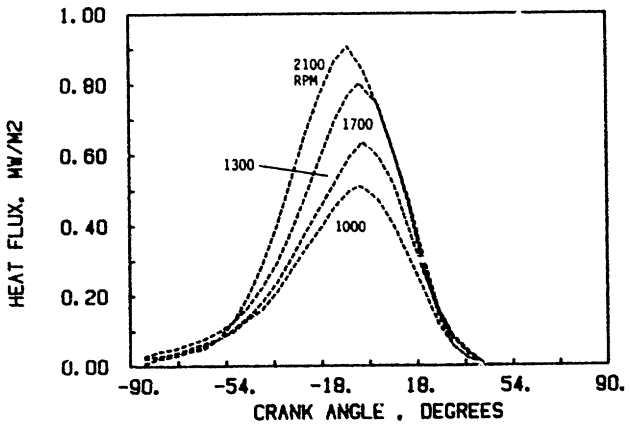

Figure 6a. Measured heat flux at bowl location, motoring operation at four engine speeds, P_{int} = P_{exh} =1.2 bar.

Fired Runs. The results obtained at the bowl position-in the fired runs are presented in Figure 7 a-d. The heat flux curves are seen to have much larger maxima than for the motored runs, in fact up to 10 times larger at the highest load levels. The heat flux is seen to be relatively low during the compression stroke, increasing relatively abruptly near TDC when the combustion begins. At each speed, the rapid increase in the heat flux occurs earlier and earlier with increasing load. This is mainly a consequence of the Cummins P-T injection system, which advances the beginning of injection as the load is increased.

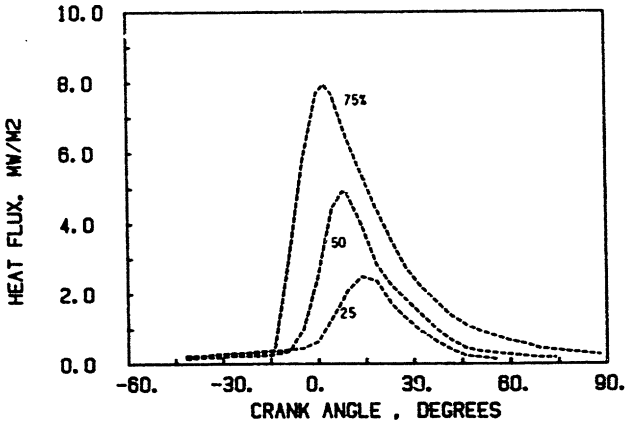

Figure 7a. Measured heat flux at bowl location, firing operation at several loads, 1000 rpm.

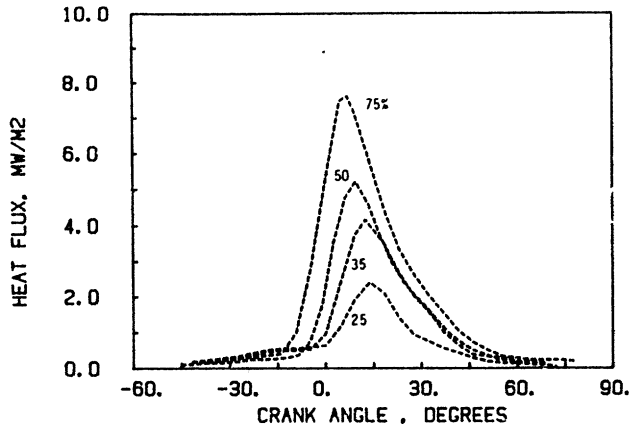

Figure 7b. Measured heat flux at bowl location, firing operation at several loads, 1300 rpm.

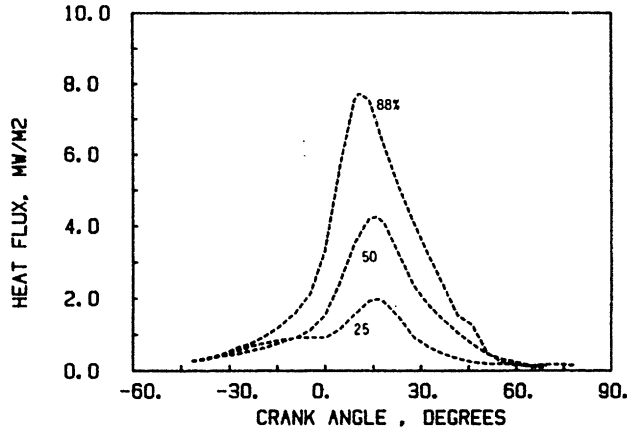

Figure 7c. Measured heat flux at bowl location, firing operation at several loads, 1700 rpm.

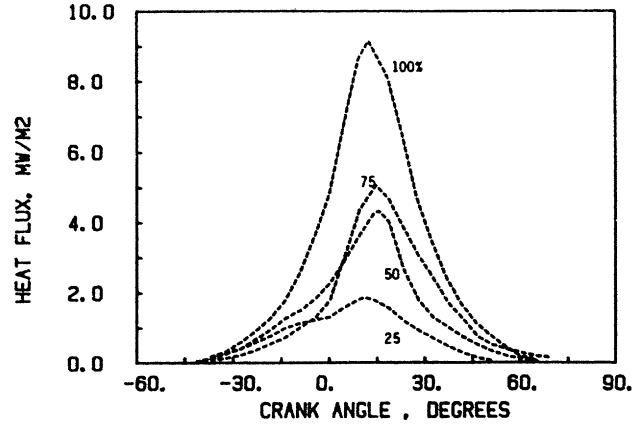

Figure 7d. Measured heat flux at bowl location, firing operation at several loads, 2100 rpm.

The heat flux measured in the crown location is shown in Figure 8 a-d. As can be seen, the heat flux in this location differs quite substantially from the bowl location. First of all, there is about a 10°CA delay in the onset of the combustion-produced heat flux increase. This is caused by the finite time it takes for the flame to propagate into the crown region. Further, the maximum heat flux levels are about two times smaller than in the bowl region, due to lower intensity of fluid flow motions in that location. This is in agreement with the observations made by Dent and Suliaman (1977) and VanGerpen et al (1985).

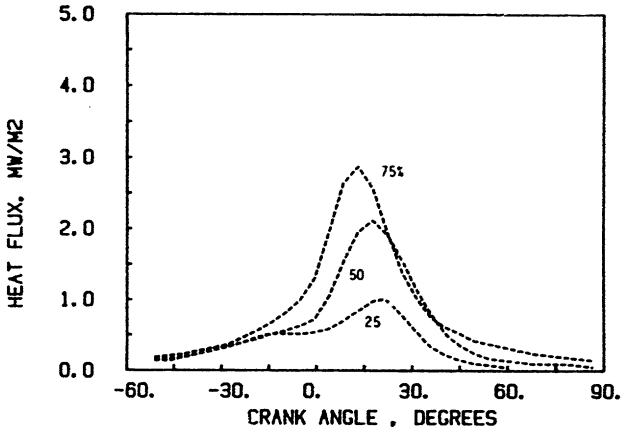

Figure 8a. Measured heat flux at crown location, firing operation at several loads, 1000 rpm.

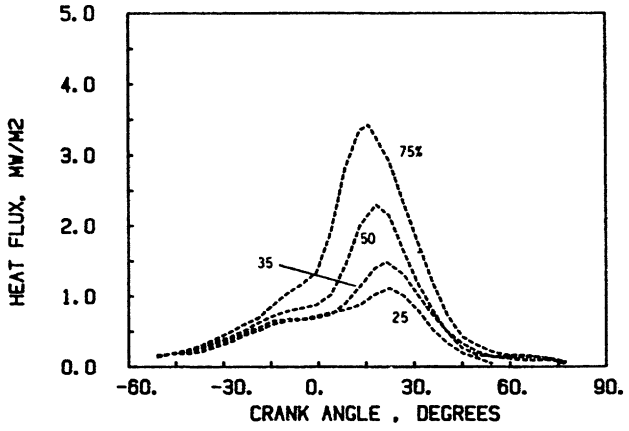

Figure 8b. Measured heat flux at crown location, firing operation at several loads, 1300 rpm.

The trends of the peak heat flux values with engine speed and load are summarized in Figure 9. It is plotted with respect to fueling rate per stroke. The fact that the data show monotonic trends over the range of speeds and loads with only a small scatter, suggests that the data set is consistent within itself and thus suitable for use in model validation.

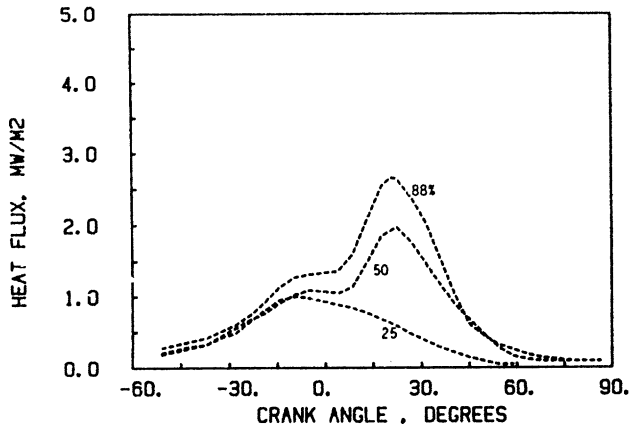

Figure 8c. Measured heat flux at crown location, firing operation at several loads, 1700 rpm.

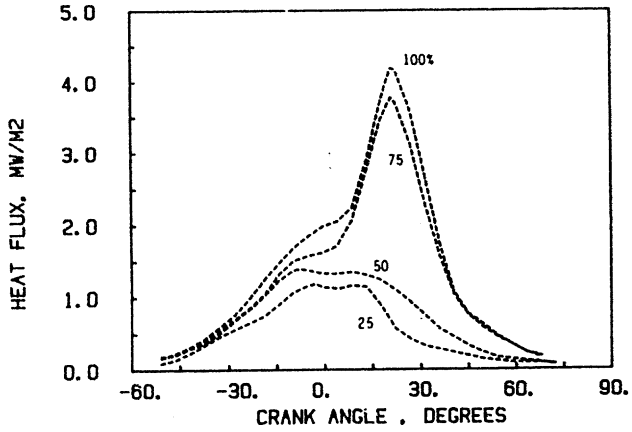

Figure 8d. Measured heat flux at crown location, firing operation at several loads, 2100 rpm.

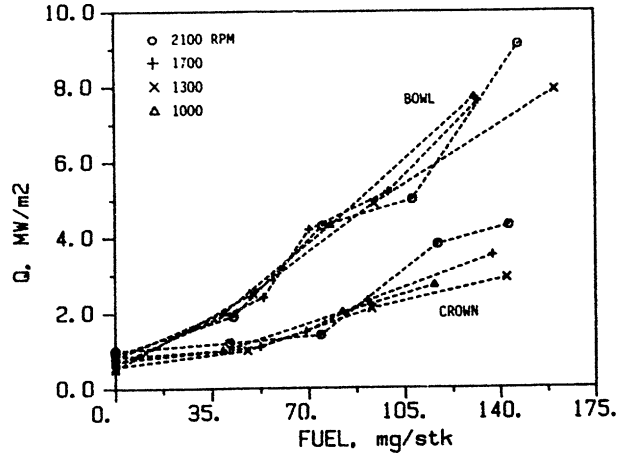

Figure 9. Measured heat flux vs. fuel/stroke at the two probe locations.

Cycle-to-cycle variations in the magnitude of the surface temperature swings were observed at both locations. A typical cycle-to-cycle variation in the crown location is shown in Figure 10. It is shown in terms of the cyclic swing ratio, defined as the cyclic thermocouple voltage swing (maximum-minimum) normalized by the average swing, averaged over 34 cycles. Although these variations can be substantial, they tend to alternate on a short time scale and thus the average over 17 or 34 cycles yielded quite repeatable results for runs performed on different days.

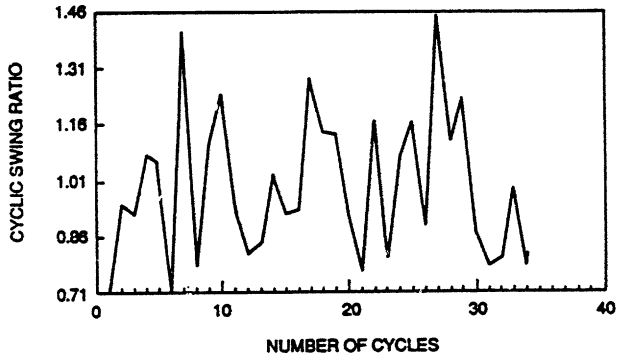

Figure 10. Typical record of cycle-to-cycle variation of peak heat flux with respect to cycle-mean peak heat flux. Crown location, 2100 rpm, 50% load.

COMPARISON OF PREDICTIONS TO DATA

Annand Correlation vs Flow-based Model. In Figure 11a are presented the data taken at the rated engine conditions (rated speed and load). The differences between the data taken at the two probe locations are seen to be quite pronounced. That was planned at the start of the experiments, and the two locations were chosen because large differences were expected between the heat fluxes there. The figure also includes a prediction obtained using Annand's correlation. It is seen that the correlation fails to show the differences between the two locations. In fact, the heat flux at the bowl location is actually lower than at the crown location, and this is due to the higher wall temperature at the uncooled valve insert location. This failure of the widely used correlations such as Annand (1963) or Woshni (1967) (Figure 11b) to represent correctly detailed features and to provide spatial resolution has been well documented in the literature, see e.g. Van Gerpen et al (1985).

By contrast, the flow-based model shows an excellent agreement with data (Figure 11c). The maximum values of the heat flux at the two locations are reproduced. Also, there is a good similarity in the shape of the heat flux at the crown location.

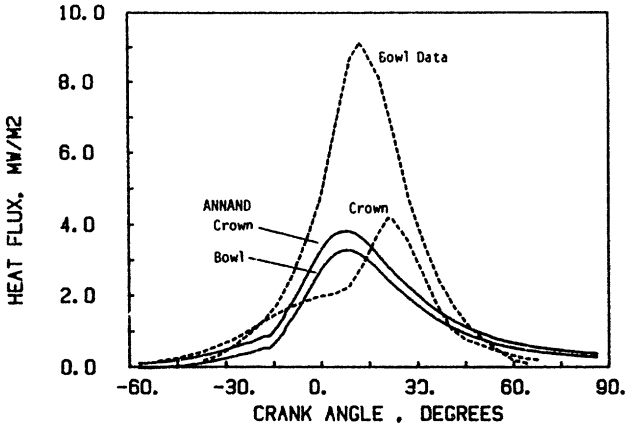

Figure 11a Heat flux at rated conditions, comparison of Annand correlation vs. data.

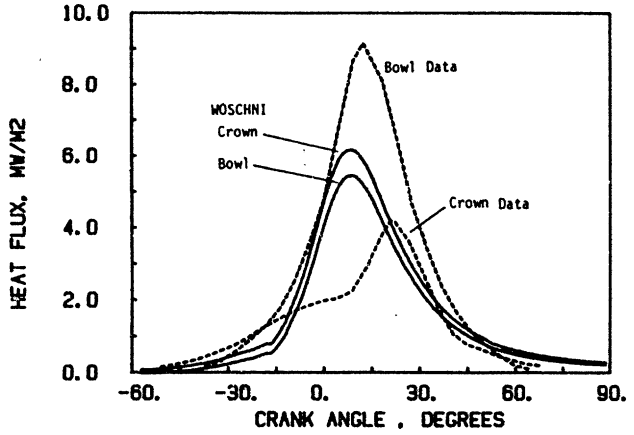

Figure 11b. Heat flux at rated conditions, comparison of Woschni correlation vs. data.

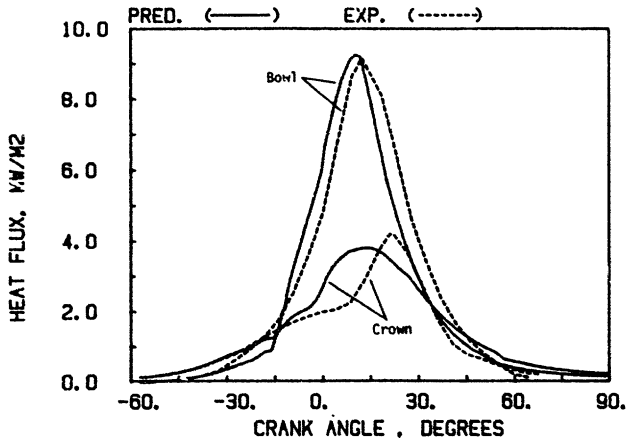

Figure 11c. Heat flux at rated conditions, comparison of flow based model vs. data.

The surface temperature swing at the bowl location at rated conditions is shown in Figure 12. Its magnitude is about 28K. The prediction shows a very good agreement with the experiment (the same material properties were used both in IRIS and in the experimental data reduction scheme), and this is not surprising in view of the agreement in the heat fluxes seen in Figure 11b.

Flow-based Model vs. Data. The agreement seen in Figure 11c extends over the entire set of data, as will be shown in the subsequent figures.

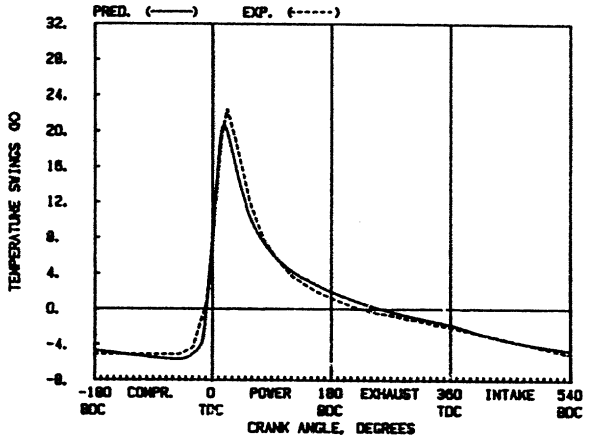

Figure 12. Wall temperature swings at the bowl location, prediction vs. data.

In motored runs, Figure 13a-b, the predictions agree with data at all speeds at both probe locations, simulating correctly the trends with speed, as well as spatial variations between the two locations. Also, the asymmetry of the heat flux curves, commented on earlier, is

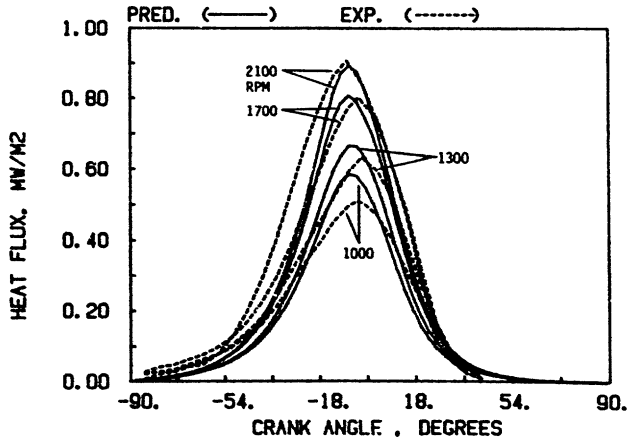

Figure 13a. Comparison of predictions and data for motoring operation, bowl location, various engine speeds, $P_{int} = P_{exh} = 1.2$ bar.

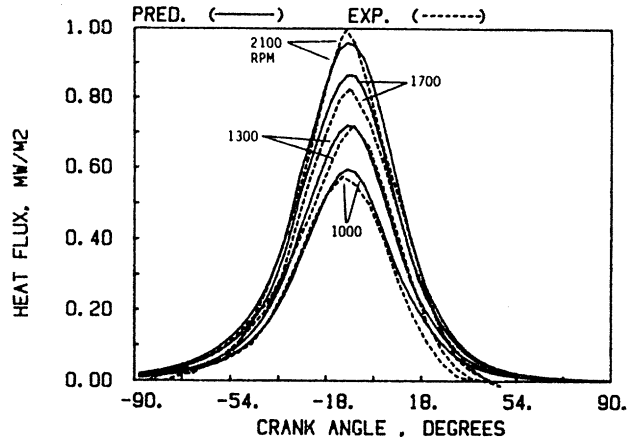

Figure 13b. Comparison of predictions and data for motoring operation, crown location, various engine speeds, $P_{int} = P_{exh} = 1.2$ bar.

predicted well as a result of a correct simulation of the rate of decay of in-cylinder flow motions.

The agreement is similarly good under firing conditions. The comparison of predictions to data is shown in Figures 14a-d for the bowl location, and in Figures 15a-d for the crown location. The model tends to show a fairly gradual and consistent change in heat flux shape and magnitude with increasing load; this is an expected behavior for a model. By comparison, the experimental curves exhibit some scatter in the trends, sometimes being somewhat below the predicted ones, sometimes above them. Overall, however, the predictions compare quite well with the data.

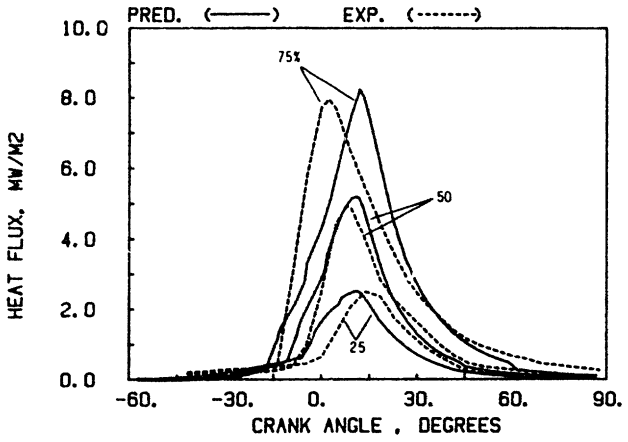

Figure 14a. Comparison of predictions and data for firing engine, bowl location, 1000 rpm. Three loads.

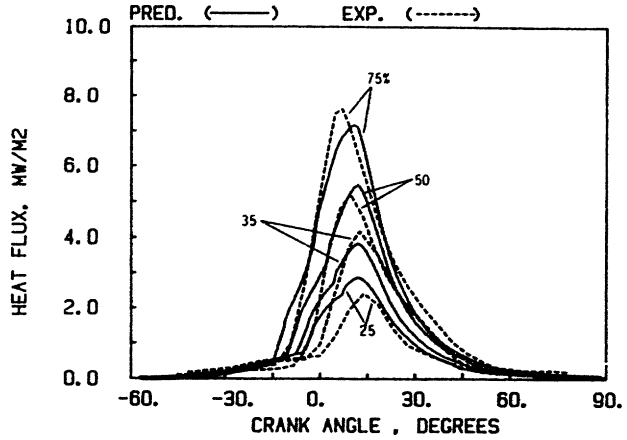

Figure 14b. Comparison of predictions and data for firing engine, bowl location, 1300 rpm. Four loads.

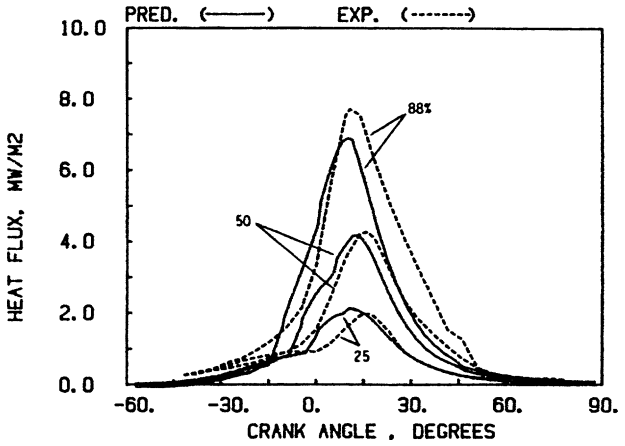

Figure 14c. Comparison of predictions and data for firing engine, bowl location, 1700 rpm. Three loads.

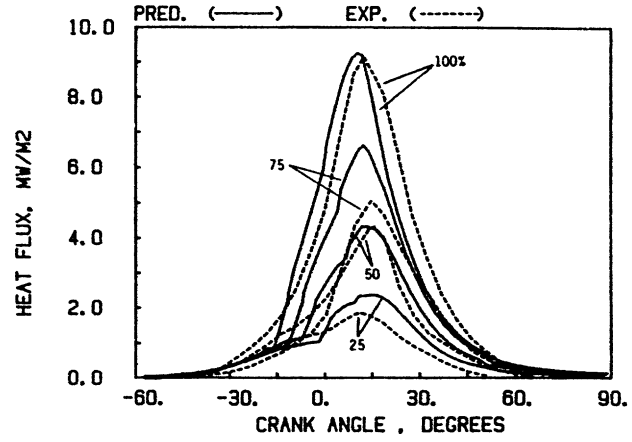

Figure 14d. Comparison of predictions and data for firing engine, bowl location, 2100 rpm. Four loads.

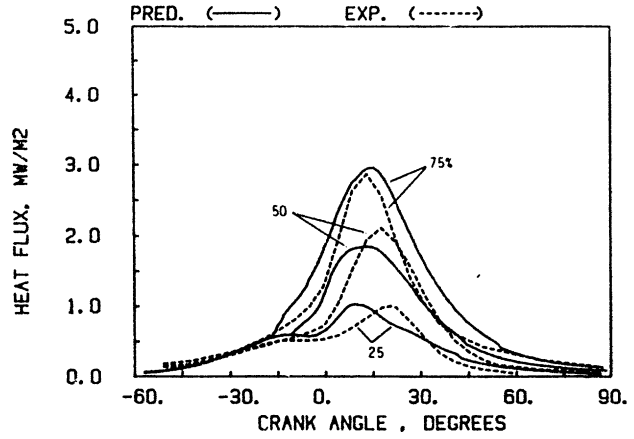

Figure 15a. Comparison of predictions and data for firing engine, crown location, 1,000 rpm. Three loads.

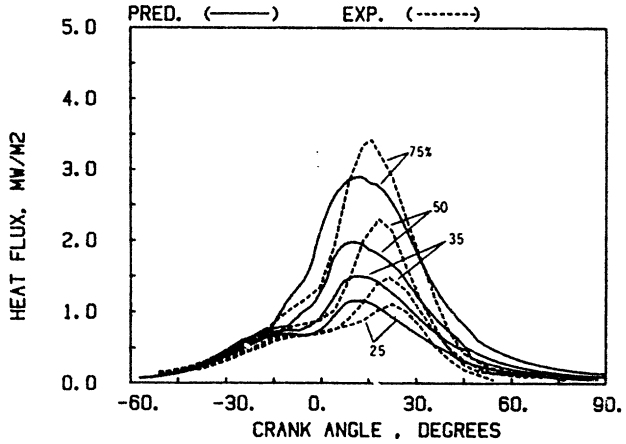

Figure 15b. Comparison of predictions and data for firing engine, crown location, 1300 rpm. Four loads.

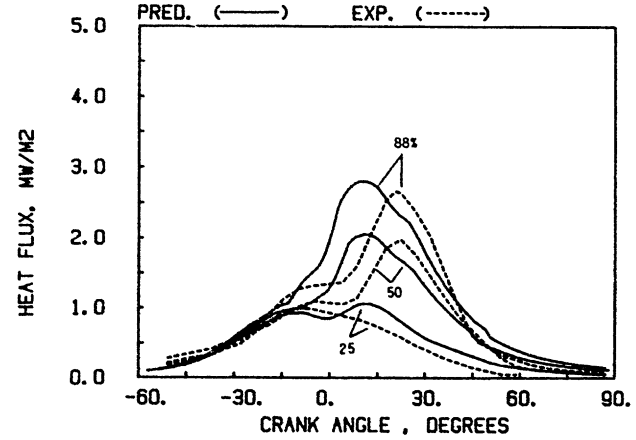

Figure 15c. Comparison of predictions and data for firing engine, crown location, 1700 rpm. Three loads.

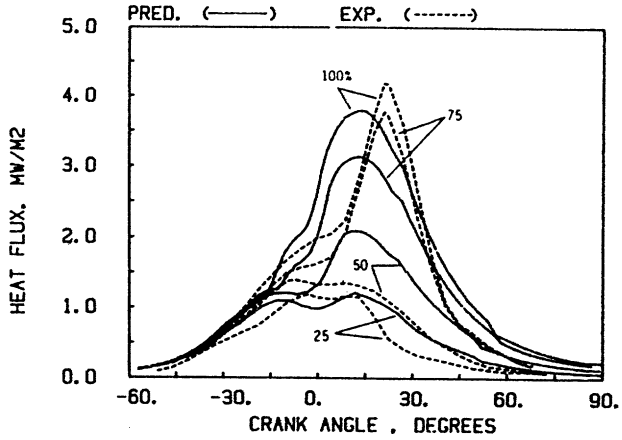

Figure 15d. Comparison of predictions and data for firing engine, crown location, 2100 rpm. Four loads.

This is also seen in Figures 16 and 17, which show the trends of peak heat flux with speed and load. The predicted curves are smooth and almost straight, while the experiments show some scatter. But again, there is a good agreement in trends and magnitude at both of the locations.

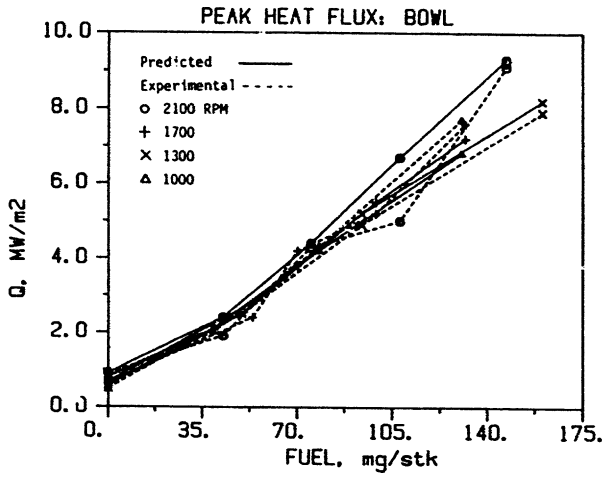

Figure 16. Comparison of predictions and data for peak heat flux, bowl location.

CONCLUSIONS

1. A comprehensive set of heat transfer data was obtained in a single cylinder D.I. diesel engine. The data is consistent and thus suitable for validation of heat transfer models.